Available online at www.sciencedirect.com
SCIENCE DIRECT®
International Journal of Solids and Structures 42 (2005) 5181–5207
INTERNATIONAL JOURNAL OF SOLIDS and STRUCTURES
www.elsevier.com/locate/ijsolstr

A cohesive model based fragmentation analysis: effects of strain rate and initial defects distribution

Fenghua Zhou *, Jean-François Molinari, K.T. Ramesh

Department of Mechanical Engineering, The Johns Hopkins University, 232 Latrobe Hall, 3400 North Charles Street, Baltimore, MD 21218, United States

Received 23 June 2004; received in revised form 8 February 2005
Available online 19 March 2005

Abstract

A one-dimensional fragmentation analysis that incorporates elastic wave propagation and a cohesive failure process is presented. An irreversible cohesive law models the internal crack nucleation and opening process, and the elastodynamic states of the intact material are calculated using the method of characteristics. Both the average fragment size and the fragment size distribution are obtained. The fragmentation of a model ceramic system is simulated over a wide range of strain rates, and the calculated results are compared to existing theoretical, numerical and experimental results. In the high strain-rate regime, the calculated average fragment size is smaller than that predicted by energy models, but at quasistatic rates the calculated average size is larger than that estimated by such models. The intrinsic mechanisms leading to these deviations are discussed. The fragment size distributions exhibit similarity under all strain-rate range. The effect of the distribution of internal defects on the fragmentation and fragment size distribution is also investigated using this methodology.

Keywords: Fragmentation; Dynamic fracture; Cohesive model; Wave analysis; Intrinsic defect

1. Introduction

Ceramics are usually brittle and have a large population of intrinsic (and extrinsic) defects. A probabilistic approach based on the *weakest-link theory* is generally used to account for the stochastic fracture properties of ceramics (Weibull, 1939a,b, 1951). However, if the external loading is applied rapidly, as when an armor ceramic system experiences a blast loading, one nucleated crack does not have sufficient time to

* Corresponding author. Tel.: +1 410 516 4398; fax: +1 410 516 4316.
E-mail address: fzhou@jhu.edu (F. Zhou).

0020-7683/$ - see front matter © 2005 Elsevier Ltd. All rights reserved.
doi:10.1016/j.ijsolstr.2005.02.009

unload a large neighborhood. Numerous cracks form, propagate and coalesce, and this dynamic multiple crack formation results in an averaging effect that invalidates the weakest-link hypothesis. A direct result of dynamic fragmentation is that the failure strength increases and becomes less stochastic when the strain rate (or loading rate) increases (Hild et al., 2003; Zhou and Molinari, 2004b). Fragment characteristics (such as average fragment size and fragment size distribution) and their dependence on strain rate and material parameters are also important issues in dynamic applications. For example, one important objective in ceramic armor design may be to obtain maximum crack density (corresponding to the smallest fragment sizes) in the "comminuted" zone, so as to dissipate the kinetic energy of the penetrator to the largest extent.

Typical analytical models for fragmentation use energy criteria to relate material properties and strain rates to fragment sizes (we refer to these as energy models). The most well known model is that of Grady (1982), who assumed that the local kinetic energy should be balanced by the energy required for creating new surfaces. This resulted in the correct prediction of decreasing fragment size with increasing strain rate. Glenn and Chudnovsky (1986) introduced a correction term accounting for the stored elastic energy before failure. Their theory is identical to Grady's in the high strain-rate region where the local kinetic energy term is dominant, whereas in the very low strain-rate (quasistatic) region the Glenn–Chudnovsky theory predicts a mean fragment size independent of strain rate.

The energy models are straightforward and reflect some important physics. They produce estimates that are qualitatively consistent with experimental observations. Nevertheless, there are two major drawbacks to these models. First, while they predict an average fragment size as a function of strain rate, they do not provide any information about the fragment size distribution (although Grady et al. (Grady and Kipp, 1985; Grady, 1990) have developed a purely geometric statistical fragmentation model). A second drawback of such models is that they usually predict a larger fragment size at high strain rates than observed in numerical simulations and in experiments (Miller et al., 1999; Wang and Ramesh, 2004). The major limitations of energy models arise from the difficulty of anticipating how much of the total energy should be dissipated in the creation of fractured surfaces.

A quantitative investigation of fragmentation necessitates detailed consideration of the dynamic fracture process, including crack nucleation, crack opening and crack interaction. Recent progress in computational techniques has made it possible to perform numerical simulations of dynamic fragmentation. In these simulations, the separation of the material is explicitly modeled by cohesive elements (Xu and Needleman, 1994, 1996, Camacho and Ortiz, 1996). Because the cohesive model treats the material separation as a process rather than as an instantaneous event, an approach that employs a cohesive model adds an intrinsic time scale to the energy release process of fracture. Other representative numerical investigations of the dynamic fracture and fragmentation phenomena have been conducted by Espinosa et al. (1998), Pandolfi et al. (1999), Miller et al. (1999), and Zhou and Molinari (2004a,b). Miller et al. (1999) specifically investigated the effect of high strain rates on fragment size; one significant finding was that the calculated fragment size was an order of magnitude finer than predicted by the energy models.

Motivated by Miller et al.'s results, Drugan (2001) developed an analytical model to investigate the fragmentation of a one-dimensional bar under uniform tensile strain rate. Drugan assumed that the fracture of the bar follows an exponential cohesive process (of the type used by Xu and Needleman, 1994), and that the fragmentation starts *simultaneously* at multiple defect points *equally spaced* along the bar. The corresponding fundamental problem involves stress wave propagation within a finite length bar with mixed boundary conditions, and solving this problem reveals the process of fragmentation. Drugan assumed that the least defect interval for which the fragmentation process can be completed corresponds to the fragment size. For most strain rates, the calculated value of the fragment size was smaller than the energy model, which agrees with the results of Miller et al. The major limitation of Drugan's model is the assumption that all cracks are formed simultaneously at equally-spaced locations. In reality cracks can initiate at many random locations and at different times. Assuming equally-spaced defects prohibits extracting information about fragment size distribution, and ignores the existence of intrinsic defect distributions.

Shenoy and Kim (2003) extended Drugan's approach to consider the fragmentation of a bar containing initial defects. They prescribed defects as *equally-spaced* cohesive node-couples, which open following the exponential cohesive law. Unlike Drugan, Shenoy and Kim analyzed a long bar that contains many (1000 or 5000) defects, the strengths of which are randomly distributed over a certain range. As the bar is deformed, the defects open and communicate with each other via stress wave propagation through non-defected regions. Thus the fragmentation process is considered as a wave propagation problem coupled with local cohesive fracture. Shenoy and Kim used two approaches to solve this problem. In the first approach, the status of each flaw was calculated by numerical integration along the characteristic lines. Each defect is only influenced by its neighboring stress state. This approach gives direct results about fragment size and size distributions. In the second approach (dynamic mean-field theory or DMFT), Shenoy and Kim introduced a dynamic mean stress, and assumed that this stress controls the growth behavior of all defects. The dynamic mean stress was calculated by integrating a compatibility equation that links the mean stress to the mean defect growth. The DMFT approach calculates fragment size that is reasonably close to the exact solution. However, the fragment size distribution given by DMFT is significantly different from the first approach, as the DMFT analysis averages the detailed growth behavior of each defect.

We adopt here a numerical approach similar in spirit to Shenoy and Kim (2003) to analyze the fragmentation of a one-dimensional bar, but extend the problem to consider a much wider range of strain rates and to explicitly incorporate spatial distributions of intrinsic defects (such as are found in real ceramics) along with various strength distributions. We are able to attain a very wide range of strain rates (including very low rates) by incorporating a new irreversible cohesive model that provides numerical stability. These two extensions allow comparisons with experimental data on real ceramics. In what follows, we first briefly describe the numerical approach, which incorporates multiple mechanisms (elastic wave propagation, local crack nucleation, opening and complete fracture of the nucleated cracks and closing and contact of partially opened cracks) in a synergistic calculation. Next, we analyze the fragmentation of a ceramic bar, and examine the rate-dependence of fragment size and fragment size distributions. The computed results are rigorously compared to available theoretical, numerical, and experimental results. It is seen that in the high strain-rate region, the average fragment size is smaller than the energy model estimates (which confirms previous numerical results), while in the low strain-rate region the calculated average fragment size is larger than estimated by the Glenn–Chudnovsky model. We then investigate the influence of initial defect distributions (both spatial and strength) on the fragmentation of a ceramic bar, and show the conditions under which these defect distributions will have a strong impact on the observed fragment distributions. Finally, we discuss the physical mechanisms that explain these results.

2. Analytic methodology

2.1. Problem definition and cohesive model

A one-dimensional bar located in the region $(-L/2, L/2)$ along the X-axis is considered. The bar is linear elastic (Young's modulus E) before fracture. At time zero ($t = 0$), the bar is intact with uniform stress σ_0 and strain $\varepsilon_0 = \sigma_0/E$, and is under uniform rate of tensile strain ($\dot{\varepsilon}_0$). At any time t ($t \geqslant 0$), the mass velocity v, strain ϵ and stress σ of the bar are functions of (X, t), where X is the Lagrangian coordinate. The initial and boundary conditions of the bar are

$$v(X,0) = \dot{\varepsilon}_0 X, \quad \sigma(X,0) = \sigma_0, \tag{1}$$

$$v(L/2,t) = v_{\mathrm{R}} = \dot{\varepsilon}_0 L/2, \quad v(-L/2,t) = v_{\mathrm{L}} = -\dot{\varepsilon}_0 L/2, \tag{2}$$

where v_{L} and v_{R} denote the prescribed left and right boundary velocity.

As the stress increases with time, a crack will initiate at any point when the following criterion is satisfied:

$$\sigma(X,t) \geqslant \sigma_c(X), \tag{3}$$

where $\sigma_c(X)$ is the local strength of the bar. A cohesive law, which links the crack's cohesive stress σ_{coh} to the crack opening distance δ_{coh} describes the growth behavior of the nucleated crack (Fig. 1). We employ a modified version of the Camacho and Ortiz initially rigid, linear decaying, irreversible cohesive law for the crack opening/closing behavior. The proposed cohesive law is

$$\begin{aligned} &\frac{\sigma_{coh}}{\sigma_c} = 1 - \frac{\delta_{coh}}{\delta_c}, \quad \text{for } \dot{\delta}_{coh} > 0, \ \ \delta_{coh} = \delta_{max}, \ \ D < 1.0, \\ &\frac{\sigma_{coh}}{\sigma_c} = 1 - \frac{\delta_{max}}{\delta_c}, \quad \text{for } \delta_{coh} < \delta_{max}, \ \ D < 1.0, \end{aligned} \tag{4}$$

where σ_c is the maximum cohesive force, identical to the local material strength in Eq. (3); δ_c is the critical opening distance of the nucleated crack. The maximum crack opening displacement that is attained, δ_{max}, is used as the internal variable that describes the damage development of the cohesive element. The first part of Eq. (4) applies when the crack is opening. The second part of (4) applies when the crack's opening distance is positive but less than δ_{max} (closing or reloading). The monotonic-increasing damage number D is defined as

$$D = \min(\delta_{max}/\delta_c, 1.0). \tag{5}$$

When D reaches unity, the cracking point is completely broken, leaving the cohesive stress to vanish at any positive δ_{coh}. At this point, the fracture energy G_c dissipated by the crack is

$$G_c(X) = \frac{\sigma_c(X)\delta_c(X)}{2}. \tag{6}$$

The present cohesive model differs from the original Camacho and Ortiz version in the unloading path. If the original closing path of Camacho and Ortiz (see Fig. 1) were followed in such a 1D analysis, a pathological situation can arise for the case of the unloading of a slightly opened crack (e.g., a freshly nucleated crack): such a crack would unload much faster on the closing path than if it were to continue on the opening path, so that a *closing* crack can unload the local stress completely before an adjacent *opening* crack has

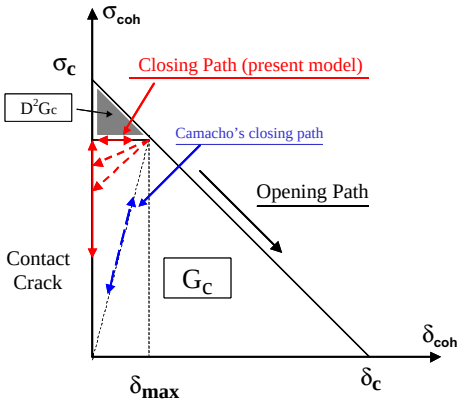

Fig. 1. Irreversible linear decaying cohesive law derived by modification of the Camacho and Ortiz model. The unloading path is flat (σ_{coh} = const. when $0 < \delta_{coh} < \delta_{max}$). Once the cohesive surfaces make contact, the point is treated as an intact point ($\delta_{coh} = 0$).

the chance to unload. The result of this pathological behavior is a significant problem with numerical stability. Note that this pathology does not arise in 2D or 3D analyses. However, for one-dimensional analyses such as in this work, a modification of the unloading path is necessary to ensure stability. We have performed a number of numerical tests to show that numerical stability is significantly improved for *any* unloading path having a slope $|\frac{d\sigma_{coh}}{d\delta}|$ that is lower than the slope of the opening path, namely σ_c/δ_c (the long-dashed lines in Fig. 1). For the purposes of further computations, we assume that as the crack unloads, the cohesive stress retains a constant value. Numerical tests have shown that the results do not change significantly with other paths that meet this stability criterion. This modification is motivated by the need for numerical stability in this one-dimensional analysis, and the need is particularly acute at low external strain rates. Use of this modification allows us to also obtain quasistatic fragment size predictions, which extends the range examined by Shenoy and Kim (2003). Physically, this concept represents a local damage state that allow the propagation of stress waves through a re-closed node and that allow subsequent damage growth to full failure.

Using this cohesive model, the fragmentation of the bar is a process in which multiple cracks nucleate, grow or close, and interact with each other. The interactions among cracks occur through stress wave propagation. This problem, which incorporates cohesive fracture modeling, is solved using the finite difference method along characteristic lines (Appendix A).

3. Effect of strain rate on fragment size

Within this section, we assume that the bar is homogeneous, with the critical failure strength $\sigma_c = 300$ MPa and the fracture energy $G_c = 100$ N/m. The material parameters assumed are those of a fictitious model ceramic, with $\rho = 2.75 \times 10^3$ kg/m^3, $E = 275$ GPa, and the elastic bar wave speed $c = 10^4$ m/s. The critical crack opening distance, calculated through Eq. (6), is 0.667 μm. The bar is of length $L = 50$ mm and is divided into 50,000 segments ($\Delta X = 1$ μm). Preliminary calculations have been conducted to determine these calculation data (Appendix B). The bar is loaded in tension at a uniform strain rate, and the response is examined for 18 different strain rates, ranging from 10 s^{-1} to 5×10^6 s^{-1}. In the high strain-rate simulations ($\dot{\varepsilon}_0 \geqslant 10^3$ s^{-1}), all of the calculations begin with $\sigma_0 = 0$ and $\varepsilon_0 = 0$. However, using the natural state as the initial condition for the low strain-rate simulations ($\dot{\varepsilon}_0 \leqslant 5 \times 10^2$ s^{-1}) would dramatically increase the computation time without significant benefit since only pure elastic response occurs, with no failure, up to stresses close to the failure stress. Thus in the low rate simulations the initial stress σ_0 is set at a level close to the failure point and a corresponding initial strain value $\varepsilon_0 = \sigma_0/E$ is used.

The stress in the bar increases linearly with time as the bar is deformed. Given that the material strength is uniform, all of the internal nodes eventually crack at the critical stress level (300 MPa). The cohesive failure process coupled with the wave propagation ensures that only a fraction of the nodes are fully broken ($D = 1.0$), separating the bar into fragments. Each fragment contains other nodes that have not been fully broken, so that each fragment contains some internal damage. Fig. 2 shows an example ($\dot{\varepsilon}_0 = 500$ s^{-1}) of the damage distribution at the end of the fragmentation process. The locations of the fully broken nodes are determined by the random nature of round off numerical error. The average fragment size $\bar{s}$ is calculated by $\bar{s} = L/N_f$, where N_f is the number of fragments. For example, the bar shown in the simulation of Fig. 2 breaks into 51 fragments, so that $\bar{s}$ is 980.4 μm.

The computed variation of the average fragment size $\bar{s}$ with the applied tensile strain rate $\dot{\varepsilon}_0$ is shown in the log–log plot of Fig. 3, together with the predictions of existing models for fragmentation. We predict an average fragment size that decreases smoothly with increasing strain rate. At very high strain rates (>10^5 s^{-1}) the curve is linear; while at low strain rates (10 s^{-1} in this simulation) the predicted curve is nearly flat, approaching a constant $\bar{s}$ value.

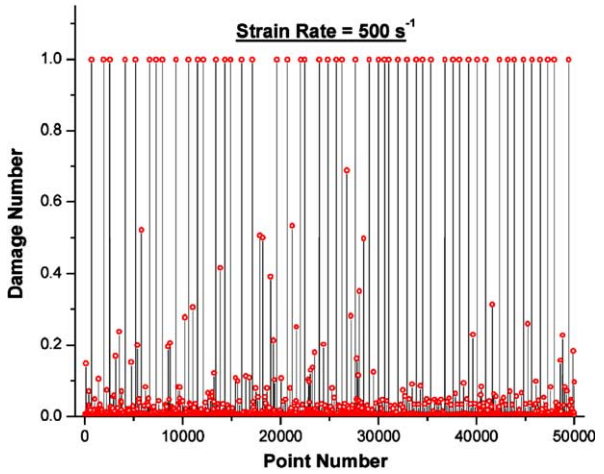

Fig. 2. Damage distribution along the 50 mm bar (strain rate = 500 s^{-1}).

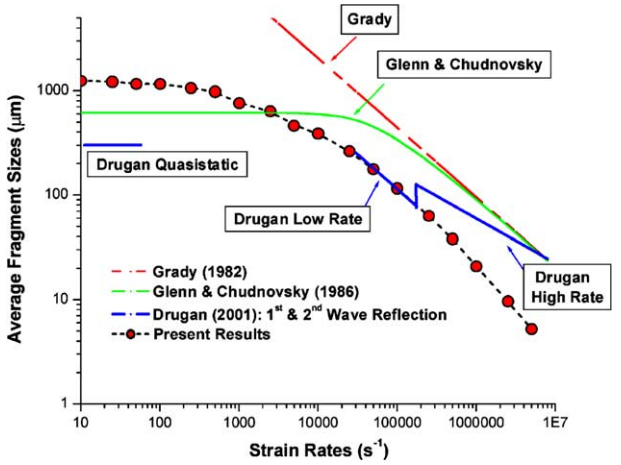

Fig. 3. Average fragment size vs. strain rate (homogeneous bar without defects).

3.1. Comparison with energy models

Miller et al. (1999) presented expressions for the fragment size in the one-dimensional uniaxial stress case according to the Grady (1982) and Glenn and Chudnovsky (1986) models.[1] Using the relationship $G_c = K_c^2/E$, these expressions are

$$\text{Grady:} \quad \bar{s} = \left(\frac{24G_c}{\rho\dot{\varepsilon}_0^2}\right)^{1/3}. \tag{7}$$

[1] The Grady's, and Glenn and Chudnovsky's results are written in a 3D setting, but the same arguments can be applied to 1D or 2D cases. Please see Appendix C for brief deductions.

$$\text{Glenn and Chudnovsky:} \quad \bar{s} = 4\sqrt{\frac{\alpha}{3}}\sinh\left(\frac{\phi}{3}\right), \tag{8}$$

where

$$\phi = \sinh^{-1}\left[\beta\left(\frac{3}{\alpha}\right)^{3/2}\right], \quad \alpha = \frac{3\sigma_c^2}{\rho E\dot{\varepsilon}_0^2}, \quad \beta = \frac{3}{2}\frac{G_c}{\rho\dot{\varepsilon}_0^2}. \tag{9}$$

Note that Glenn and Chudnovsky's theory gives a quasistatic fragment size estimate:

$$\bar{s}_{\text{quasistatic}}\big|_{\text{Glenn–Chudnovsky}} = \frac{4\beta}{\alpha} = \frac{2EG_c}{\sigma_c^2}. \tag{10}$$

These theoretical curves are also presented in Fig. 3 for comparison. Our numerical results for the average fragment size exhibit similar trends to that anticipated by Glenn and Chudnovsky, but are quantitatively different over the entire strain rate range. In the low strain-rate region ($10-10^3\ \text{s}^{-1}$), our calculated average fragment size (1250 μm) is about twice the value of $\bar{s}_{\text{quasistatic}}|_{\text{Glenn–Chudnovsky}}$, which is 611 μm. In the high strain-rate region ($>10^5 s^{-1}$), however, our fragment sizes are smaller by a factor of approximately 5. These differences can be understood in terms of energetics as follows. At low strain rates, where strain energy is the dominant influence on fragmentation, our results imply that approximately half (certainly not all) of the strain energy stored in the bar before fracture is used for the creation of new crack surfaces. This is to be expected, because when the bar begins to break, the sudden stress release causes wave propagation, and so part of the stored energy is converted into kinetic energy rather than being used for new crack surface creation. In the high strain-rate region, where the kinetic energy is the dominant source of energy for the creation of new crack surfaces our results show that additional energy sources, either external work, or the *global* kinetic energy must be contributing to create additional fracture surfaces (the Grady and Glenn–Chudnovsky models assume that only the *local* kinetic energy is used for fracture at the high rates).

Fig. 4 presents the computed history of the kinetic energy K_E, the strain energy P_E, the fracture energy F_E, and the external work W of the system for the "quasistatic" strain-rate ($\dot{\varepsilon}_0 = 10\ \text{s}^{-1}$). The stored strain energy decreases precipitously as soon as the bar begins to fail. Simultaneously, the kinetic energy and the fracture energy increase, as does the number of fragments (not shown in the figure); the external work has

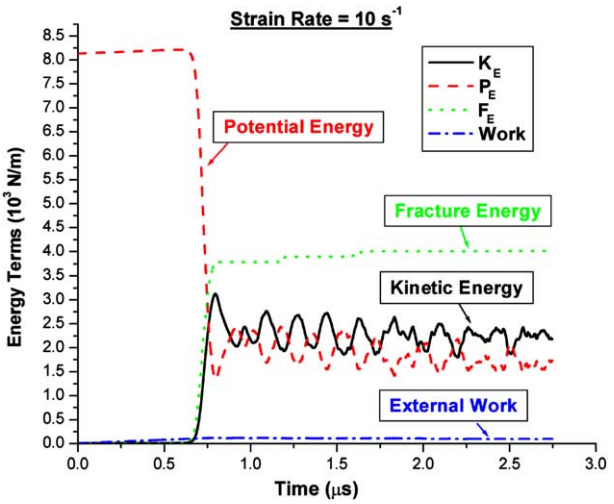

Fig. 4. Energy history curves in quasistatic loading case ($\dot{\varepsilon}_0 = 10\ \text{s}^{-1}$).

little contribution to the system's total energy. Once the number of fragments saturates, F_E is constant and K_E and P_E oscillate (reflecting the elastic waves trapped in the fragments). The conservation of total system energy gives $P_E(0) \approx (K_E + P_E) + F_E$ where $P_E(0)$ is the stored strain energy before failure. For this quasistatic case our results show that $(K_E + P_E)$ and F_E each account for approximately 50% of $P_E(0)$ (the fracture energy consumed by the partially opened internal points is only 2–3% of F_E). Since roughly half of P_E is used to break the bar, the computed average fragment size is twice as large as the Glenn–Chudnovsky estimate, and so the quasistatic fragment size is given by

$$\bar{s}_{\text{quasistatic}} = 2\bar{s}_{\text{quasistatic}}\big|_{\text{Glenn–Chudnovsky}} = \frac{8\beta}{\alpha} = \frac{4EG_c}{\sigma_c^2}. \tag{11}$$

3.2. Comparison with dynamic models

Drugan (2001) developed an empirical scaling law that links the non-dimensional fragment size to the non-dimensional strain rate. Drugan's theory is based on an exponential-type cohesive law, while we use a different cohesive law. Since the critical cohesive stress and the cohesive energy are physical quantities, the characteristic crack opening distance in the exponential cohesive law is related to our δ_c by $\delta^* = G_c/e\sigma_c = \delta_c/2e$ (e is the natural logarithm base). Drugan's scaling law may be rewritten as

$$\frac{\bar{s}}{\left(EG_c/2e\sigma_c^2\right)} = 2.1395\left[\frac{\dot{\varepsilon}_0}{\left(2ec\sigma_c^3/E^2G_c\right)}\right]^{-0.4264} \quad \text{if } \dot{\varepsilon}_0 > 0.9120\left(2ec\sigma_c^3/E^2G_c\right), \tag{12}$$

$$\frac{\bar{s}}{\left(EG_c/2e\sigma_c^2\right)} = 1.2999\left[\frac{\dot{\varepsilon}_0}{\left(2ec\sigma_c^3/E^2G_c\right)}\right]^{-0.66671} \quad \text{if } \dot{\varepsilon}_0 < 0.9120\left(2ec\sigma_c^3/E^2G_c\right). \tag{13}$$

Drugan's results are also plotted in Fig. 3, and agree well with our results in the intermediate strain-rate region. However, Drugan's results differ from ours at both low and high strain rates. In the high strain-rate region, Drugan's fragment size approaches and eventually exceeds the energy model estimates. Our model predicts a smaller average fragment size at all high strain rates, with a greater slope than the energy model. This difference between our results and Drugan's results is because Drugan assumed that the fragmentation process is initiated simultaneously at all sites and that all fragment sizes are equal, while in our model the fragmentation process is randomly determined and the fragment sizes can vary. Thus in our model, the small fragments break within the time of one wave reflection, but the larger fragments can break over a longer time period, after multiple wave reflections. As a result, many more fragments can be created and the average fragment size is smaller at high strain rates. At low strain rates (the "quasistatic" limit) Drugan's scaling law does not apply, because it assumes one (corresponding to Eq. (12)) or two (corresponding to Eq. (13)) wave reflections before complete fracture. When more wave propagations are involved, the analysis becomes complex. Drugan did provide the following solution for the average fragment size when the loading rate is very slow:

$$\bar{s}_{\text{quasistatic}}\big|_{\text{Drugan}} = \frac{EG_c}{\sigma_c^2}, \tag{14}$$

which is half the Glenn–Chudnovsky quasistatic size and one-fourth of our model prediction. Among the quasistatic fragment size predictions: (10), (11) and (14), we consider our value (11) to be the best estimate since it explicitly handles the energetics and the dynamics, as well as allowing for random fragmentation and variable fragment size. Finally, we note that Drugan's results show discontinuities (jumps) in the $\bar{s}$–$\dot{\varepsilon}_0$ curve as a result of transitions between the n-wave reflection and $(n+1)$-wave reflection cases. Our

analysis does not have this drawback. As can be seen in Fig. 3, except for some minor numerical fluctuations, the calculated $\bar{s}$–$\dot{\varepsilon}_0$ relationship is a smooth, monotonically decreasing curve.

The model of Shenoy and Kim (2003) has many of the features of our analysis, and their computed average fragment size displays the same trend with strain rate as in our results in the *intermediate to high strain rates*. Although direct comparisons of our results with those of Shenoy and Kim are difficult because both the cohesive model and the material parameters used in our analysis differ significantly from those used by Shenoy and Kim, we can compare these results indirectly using Grady's estimation as a common measure. Shenoy and Kim's fragment size is dependent on the initial defect weakness, $\Delta\sigma_0/\sigma_0$. The case $\Delta\sigma_0/\sigma_0 = 10^{-5}$ is close to our results shown in Fig. 3. In the strain-rate region 6×10^3–10^5 s^{-1}, Shenoy and Kim's fragment size is about 1/20 to 1/4 of Grady estimation. Simultaneously, our fragment size is 1/20 to 1/4 of Grady estimation in strain-rate region 5×10^2–10^4 s^{-1}. Considering the fact that our material is more ductile (with larger G_c and smaller σ_c values) than Shenoy and Kim's, the two results are quite close to each other when the strain rate is translated one order of magnitude. Shenoy and Kim did not report any results in the quasistatic case and thus the comparison is limited to intermediate to high strain rates.

3.3. Energy dissipated by partially opened cracks

As shown in Fig. 2, residual damage exists along the fragmented bar after fragmentation finishes. These damaged but not fully broken points dissipate additional energy during the fragmentation process. For the cohesive law illustrated in Fig. 1, the energy dissipated by a cohesive point with damage number D is the area of the shaded region:

$$g_{\text{coh}} = D^2 G_c. \tag{15}$$

During the fragmentation process, the total fracture energy F_E and the part of it consumed by partially opened cracks F_D are

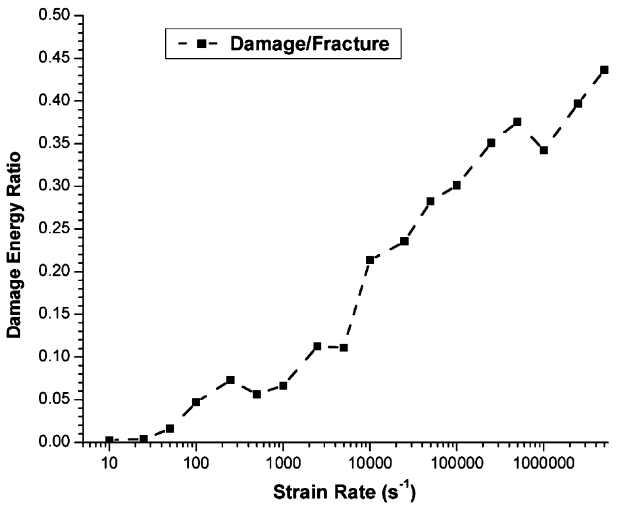

Fig. 5. Ratio of cohesive energy consumed by partially broken nodes with total cohesive energy.

$$F_{\mathrm{E}} = \sum_{i=1}^{N-1} g_{\mathrm{coh}}(i) = G_{\mathrm{c}} \sum_{i=1}^{N-1} D(i)^2,$$
$$F_{\mathrm{D}} = F_{\mathrm{E}} - G_{\mathrm{c}} \sum_{i=1, D(i)=1}^{N-1} D(i)^2 = G_{\mathrm{c}} \left[\sum_{i=1}^{N-1} D(i)^2 - (N_{\mathrm{f}} - 1) \right]. \tag{16}$$

The ratio of damage energy F_{D} to total cohesive energy F_{E} is plotted against strain rate in Fig. 5. It is seen that there is an increasing trend of internal damage generation for increasing loading rate. Within the quasi-static region ($\dot{\varepsilon}_0 < 500\ \mathrm{s}^{-1}$), $F_{\mathrm{D}}/F_{\mathrm{E}}$ is less than 5%, so that the energy dissipated by the damaged internal nodes is negligible. However, at the high strain-rate end ($5 \times 10^6\ \mathrm{s}^{-1}$), $F_{\mathrm{D}}/F_{\mathrm{E}}$ is approaching 50%, so that the energy dissipated in the damaged nodes is very significant at high strain rates.

4. Statistics of fragment size

A significant merit of the present analytical approach is that fragment size statistics are the output of the calculation. Although all the internal points have identical material properties, the size of each fragment is not necessarily the same because of the random nature of the fragmentation process. This section discusses the statistical characteristics of fragment sizes. Although the statistical data are all presented for a single material, the results can be extended to other materials with different parameters—such an extension is provided in a subsequent paper for reasons of space.

Results from six fragmentation simulations, with strain rates $10^1\ \mathrm{s}^{-1}$, $10^2\ \mathrm{s}^{-1}$, $10^3\ \mathrm{s}^{-1}$, $10^4\ \mathrm{s}^{-1}$, $10^5\ \mathrm{s}^{-1}$, and $10^6\ \mathrm{s}^{-1}$, are analyzed. The total fragment numbers N_{f} are 40, 43, 66, 128, 433, and 2397 respectively. The size of each fragment is independent of the fragment location. The length of fragment i is denoted by s_i, and the average fragment size is then:

$$\bar{s} = \frac{1}{N_{\mathrm{f}}} \sum_{i=1}^{N_{\mathrm{f}}} s_i = \frac{L}{N_{\mathrm{f}}}. \tag{17}$$

As the strain rate increases, the average fragment size decreases, while the relative size span increases. A function called the cumulative fragment number, $\Phi(s)$, is defined as the number of fragments that have sizes larger than s (Grady and Kipp, 1985):

$$\Phi(s) = \sum_{i=1}^{N_{\mathrm{f}}} \mathbf{L}(s_i \geqslant s), \tag{18}$$

where $\mathbf{L}(\mathbf{S})$ is the logical function. $\mathbf{L}(\mathbf{S}) = 1$ if statement $\mathbf{S}$ is *true*, and $\mathbf{L}(\mathbf{S}) = 0$ if $\mathbf{S}$ is *false*.

$\Phi(s)$ is a monotonically decreasing function, with two boundary values:

$$\Phi(s_0) = N_{\mathrm{f}}, \quad \Phi(\infty) = 0, \tag{19}$$

where s_0 is the minimum fragment size. The number of the fragments within the size range $s \to s + \mathrm{d}s$ is $-\Phi'(s)\,\mathrm{d}s$. Making use of the boundary values shown in Eq. (19), we have:

$$L = \int_{s_0}^{\infty} [-s\Phi'(s)]\,\mathrm{d}s = s_0 N_{\mathrm{f}} + \int_{s_0}^{\infty} \Phi(s)\,\mathrm{d}s. \tag{20}$$

Eq. (20) is a geometric property of the cumulative fragment number function.

At each strain rate, we normalize the size of each fragment s_i by the average size $\bar{s}$, then sort these values in descending order to obtain the cumulative fragment number function $\widetilde{\Phi}(s/\bar{s}) = \Phi(s)$. The resulting $\widetilde{\Phi}(s/\bar{s})$ functions are presented in the semi-logarithm plot of Fig. 6a for all strain rates, together with the total number of fragments that are developed. Several observations are made from this figure:

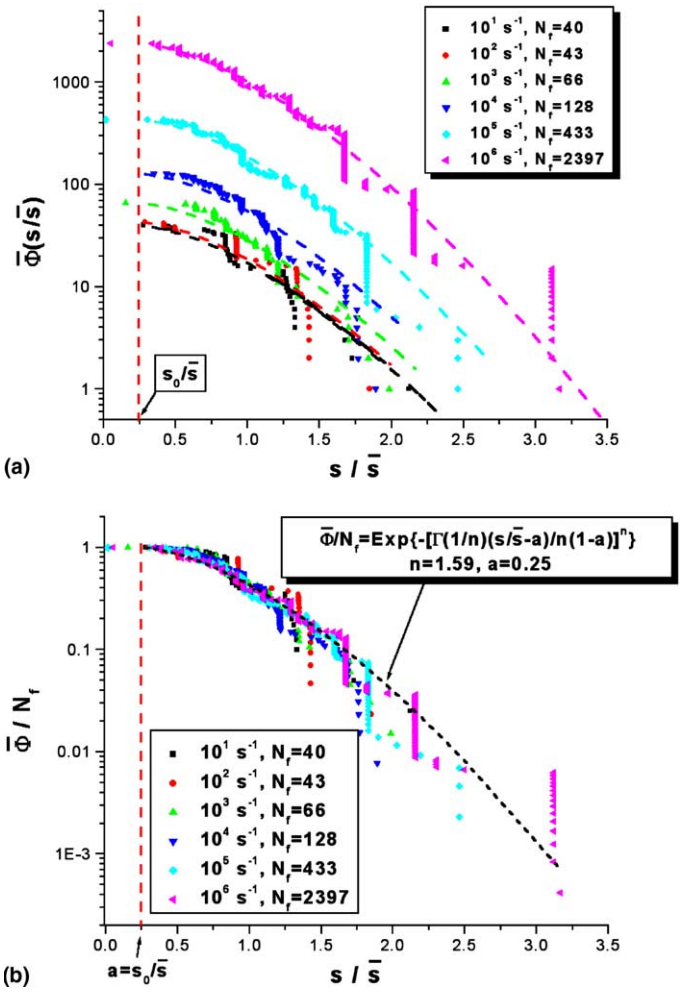

Fig. 6. (a) Cumulative fragment number curves for a range of different strain rates; (b) normalized fragment number curve for all strain rates.

1. Higher strain rate loading results in smaller fragment sizes (see Fig. 3) and wider *normalized* fragment size distributions.
2. For all strain rates, the $\log(\widetilde{\Phi})$ vs. $s/\bar{s}$ curves exhibit a similar convex shape. This is different from the suggestions of Grady and Kipp (1985) that the fragment distribution is either a linear exponential type (a straight line in the $\log(\widetilde{\Phi})$–$s/\bar{s}$ plane), or a bilinear exponential type (a concave curve in the $\log(\widetilde{\Phi})$–$s/\bar{s}$ plane).
3. In our simulation, the smallest possible fragment size is ΔX (1 μm). However, the chance that these small fragments appear is very small (we observe one or two events in the high strain-rate cases). Most of the fragments are larger than a critical size (s_0, which varies with rate of loading) and much larger than ΔX.
4. The normalized minimum fragment size $s_0/\bar{s}$ seems to be essentially independent of strain rate, at a value of about 0.25. We note that although the normalized value $s_0/\bar{s}$ is constant, the minimum fragment size s_0 decreases with strain rate.

Based on these observations, we propose that the cumulative fragment number function $\Phi(s)$ takes the following form:

$$\Phi(s) = \begin{cases} N_f & (s \leqslant s_0), \\ N_f \exp\left[-\left(\frac{\Gamma(1/n)}{n}\right)^n \left(\frac{s-s_0}{\bar{s}-s_0}\right)^n\right] & (s > s_0), \end{cases} \tag{21}$$

where n is a positive index that controls the fragment size distribution and Γ is the Gamma function. The case with $s_0 = 0.0$, $n = 1$ represents the linear exponential distribution that has been used by Grady and Kipp (1985). Evidently Eq. (21) satisfies the boundary conditions and the geometric property (Eqs. (19) and (20)). It appears (Fig. 6a) that $s_0/\bar{s}(\equiv a)$ is independent of strain rate. We assume that n is also independent of strain rate. This then results in a unified relation between $\widetilde{\Phi}/N_f$ and $s/\bar{s}$ for all strain rates, and we plot the computation results as data points in the $\log(\widetilde{\Phi}/N_f) - s/\bar{s}$ space in Fig. 6b. We find that these points lie approximately along a universal power curve:

$$\ln\left[\frac{\widetilde{\Phi}(s/\bar{s})}{N_f}\right] = -\left[\frac{\Gamma(1/n)(s/\bar{s}-a)}{n(1-a)}\right]^n \quad (s > s_0). \tag{22}$$

The parameters that best fit the numerical data are $a = 0.25$, $n = 1.59$. Substituting these parameters into Eq. (21), the fitted curves $\Phi(s)$ corresponding to different strain-rate cases are drawn in Fig. 6a (dashed lines). It is seen that with only two parameters, the cumulative fragment number functions are successfully captured. The corresponding *unified probability density function* (UPDF) of the normalized fragment size $s/\bar{s}$ is

$$\text{UPDF} = -\frac{\Phi'(s)\,\mathrm{d}s}{N_f\,\mathrm{d}(s/\bar{s})} = \begin{cases} 0 & (s \leqslant s_0), \\ n(s/\bar{s}-a)^{n-1}\left[\frac{\Gamma(1/n)}{n(1-a)}\right]^n \exp\left\{-\left[\frac{\Gamma(1/n)(s/\bar{s}-a)}{n(1-a)}\right]^n\right\} & (s > s_0). \end{cases} \tag{23}$$

This probability density function is found to adequately represent the numerical results for all normalized fragment sizes (for all strain-rate cases, over 3100 data points in total).

We now apply the unified PDF function to estimate fragment size distributions for different strain rates from quasistatic ($\dot{\varepsilon}_0 \leqslant 10^2\ \mathrm{s}^{-1}$) to $10^5\ \mathrm{s}^{-1}$, and the resulting fragment size distributions are shown in Fig. 7a. The shapes of the fragment size distribution curves and the changes in shape of the fragment size distributions with strain rate are qualitatively similar to the experimental results of Lankford and Blanchard (1991) and Wang and Ramesh (2004). In Fig. 7b we plot the fragment size (particle length) distributions of Wang and Ramesh (2004), obtained for SiC–N ceramics that are crushed under quasistatic (MTS) or impact (Kolsky bar) loadings. We note that in the experiments the SiC–N specimen generally crushes under a compressive stress (about 6 GPa) that is one order higher than the tensile strength (around 300 MPa). Therefore significant strain energy has been accumulated in the specimen before it fails. Although the failure of a specimen is triggered by compressive fracture, this compressive failure always accompanies a rapid energy release that results in dynamic tensile fragmentation. Since the specimen breaks into many pieces simultaneously, it is likely that the Weibull modulus of the material (which is derived from its quasistatic tensile or bendbar strength and is related to the largest intrinsic defect) has only a minor effect on the fragmentation behavior.[2] Therefore the simulations in this paper remain qualitatively reasonable for examining the compressive fragment statistics, particularly at higher strain rates where the kinetic energy is the dominant term.

[2] We will discuss this issue further in the next section.

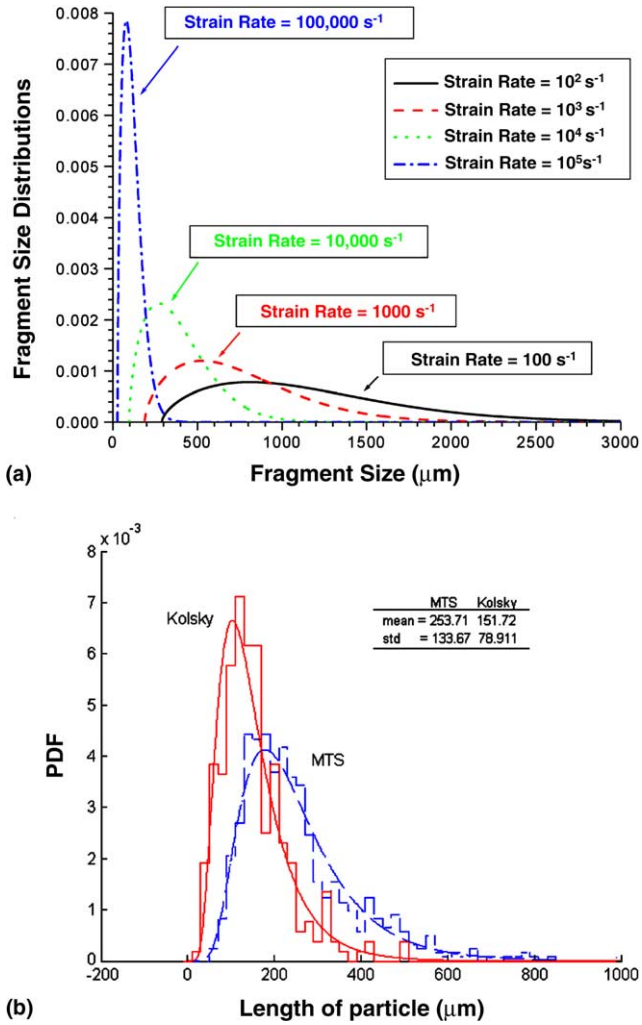

Fig. 7. (a) Fragment size distribution for various strain rates using the unified probability density function; (b) size distributions of SiC–N under quasistatic (MTS) and dynamic (Kolsky bar) compressive loadings (Wang and Ramesh, 2004).

5. Effect of internal defects distribution

In the previous section, we assumed that the bar was homogeneous and thus all internal points along the bar were activated as cohesive points when the loading level exceeded the local strength level (everywhere σ_c). In this section, we investigate the influence of internal defects distribution. Our numerical scheme allows the consideration of microstructure through a local strength distribution $\sigma_c(X)$ and a fracture energy distribution $G_c(X)$. A defect is characterized as a single point or a group (zone) of points where the local failure strength is reduced. We consider two kinds of spatial distributions of these strength defects: defects that are equally spaced along the bar, and defects that are randomly distributed along the bar. In the latter case we also allow the defect strengths to be randomly distributed, whereas for the equally-spaced defects, the defect strengths are deterministic.

5.1. Equally-spaced defect distributions

We consider two approaches to characterize an equally-spaced defect microstructure. In the first approach a defect is treated as a single isolated weakened point (a point defect). In the second approach a defect is treated as a weakened zone where the strength of a point is correlated to its immediate neighbors (a zone defect). Fig. 8 illustrates these two defect models. We assume that at the weakest defect points both the local strength σ_c and the fracture energy G_c are reduced by a factor of 50%. A total of 50 internal defect points are equally spaced at 1 mm intervals. In the point defect model the isolated defect points are located at (± 0.5 mm, ± 1.5 mm, ..., and ± 24.5 mm). In the zone defect approach the local strength linearly increases from 150 MPa (the weakest point) to 300 MPa (the intact material) over a span of 0.25 mm. The zone defect distribution can be viewed as a weakened microstructure with a characteristic length of 0.5 mm.

5.1.1. Effect of equally-spaced point defects on fragmentation

Consider first the effect of equally-spaced point defects on the fragmentation process. Fig. 9 presents the histories of the average stress ($\sigma_{ave}(t) = \frac{1}{N+1}\sum_{i=1}^{N+1}\sigma_i(t)$) across the bar and the number of fragments for three different strain rates ($\dot{\varepsilon}_0 = 10^2\ s^{-1}$, $10^4\ s^{-1}$, and $10^6\ s^{-1}$). In each case, when the bar begins to deform, the average stress increases linearly with time (and is initially equal to the local stress). At some time the local stress at the point defects reaches their critical strength level of 150 MPa, and cracks are initiated at these points. What happens subsequently differs for each rate of deformation.

At the relatively low strain rate of $10^2\ s^{-1}$ (Fig. 9a), the average stress begins to fall almost immediately after the point defects begin to decohere, and so the effective failure strength of the bar (the peak average stress $\sigma_{peak} = \max[\sigma_{ave}(t)]$) is approximately 150 MPa (which is the defect strength). Because of the cohesive model and the wave-mediated communication between points, it takes some time after the defects are initiated before full fragments develop, and only 28 of the point defects develop into completely fractured points. The final fragment number in this case is 29.

For a higher strain rate of $10^4\ s^{-1}$, we obtain the results shown in Fig. 9b. Now the average stress in the bar continues to rise even after the point defects have initiated failure, as the strain rate is higher. Eventually the unloading waves released from the defects causes the average stress to reach a maximum, and this peak strength is now about 200 MPa. The bar itself is not broken until a later time, when in this case all 50 of the point defects are completely broken, so that the number of fragments becomes 51. This is a special

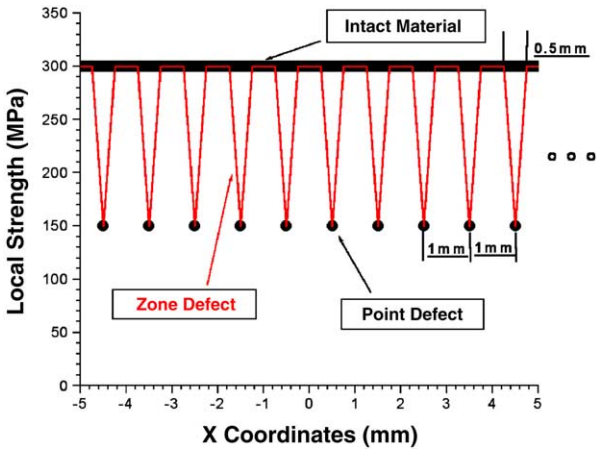

Fig. 8. Local strength distribution along the bar with no defects, equally-spaced point defects, and equally-spaced zone defects. Only part of the bar (-5 mm $\leqslant X \leqslant 5$ mm) is shown.

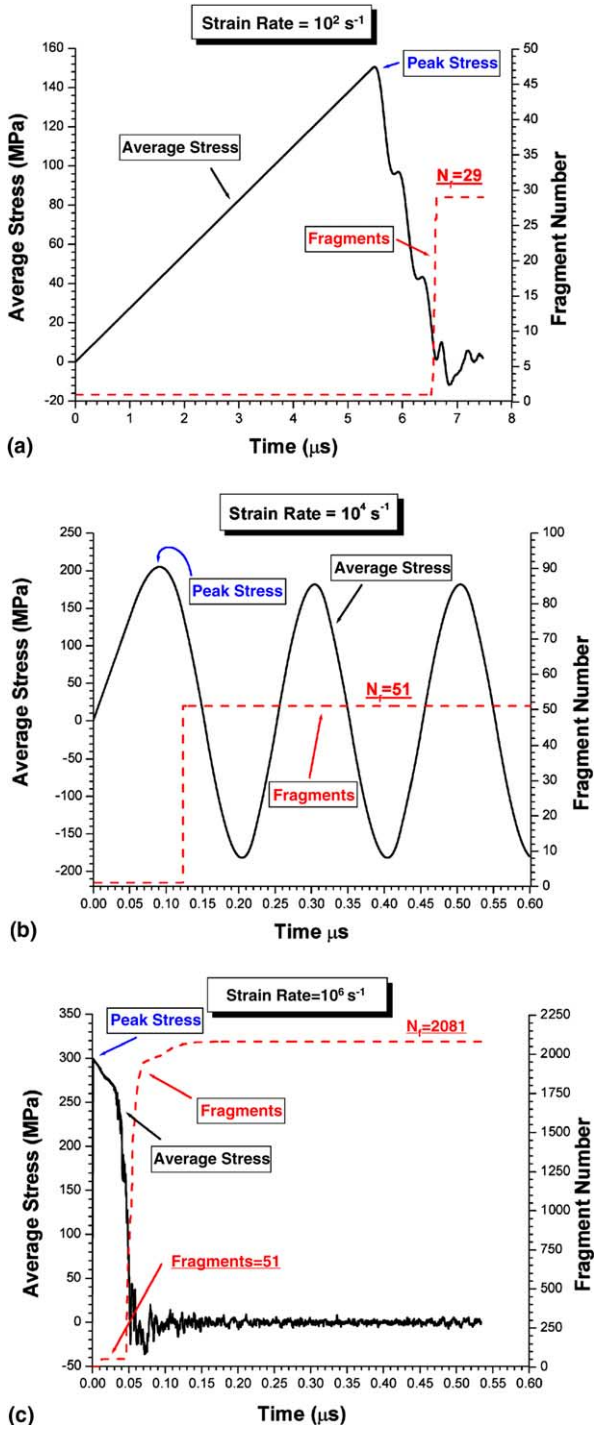

Fig. 9. Histories of the average stress in the bar and fragment number for a bar that carries equally-spaced point defects: (a) $\dot{\varepsilon}_0 = 10^2\ \mathrm{s}^{-1}$; (b) $\dot{\varepsilon}_0 = 10^4\ \mathrm{s}^{-1}$; (c) $\dot{\varepsilon}_0 = 10^6\ \mathrm{s}^{-1}$.

case, because the cracks are only initiated at the weak points, all develop into complete fracture (unlike at the lower rate), and no further fragmentation occurs (unlike at the higher rate described et seq.). No further fragments are created, even though waves continue to reverberate within the fragments (the average stress in the bar is observed to oscillate due to these internal wave reflections). The fragment number equals exactly the number of defects, and the fragment size equals exactly the defect spacing.

When a very high strain rate of $10^6\ s^{-1}$ is considered, the results shown in Fig. 9c are obtained. Now the load in the bar rises very quickly, and a peak strength (failure strength of the bar) of approximately the intact strength (300 MPa) is developed. The elastic portion of the response occurs over a time so short that it is not evident in this figure. Sufficient kinetic energy is now available to create many fragments. As before, after the local stress level exceeds 150 MPa, the 50 defect points initiate, and are eventually developed into complete fracture points (thus, the fracture number first reaches a level of 51). Many more fragments are subsequently developed within the bar at initially intact full strength locations. The final fragment number in this case is about 2080.

We have conducted simulations for 18 loading cases for a bar with such equally-spaced point defects, with strain rates ranging from $10\ s^{-1}$ to $5\times10^6\ s^{-1}$. The results are presented as the circles in Fig. 10, which shows the logarithm of average fragment size $\bar{s}$, and the peak stress σ_{peak}, as functions of the logarithm of the strain rate. The figure also presents results from other defect distributions, presented et seq. Examining only the equally-spaced point defect results, it appears that there exist three strain-rate regions that influence the fragment size differently:

1. The quasistatic region ($\dot{\varepsilon}_0 < 250\ s^{-1}$). In this region, the fragments are formed by *part* of the internal defect points that are completely broken. Other internal defect points nucleate as damaged points but are not fully opened. The failure strength of the bar is approximately the minimum value of the local strength, $\sigma_{\min}$ (=150 MPa), so that the weakest link of the bar controls the failure strength. The average size of the fragments is approaching the quasistatic estimate, Eq. (11), which assumes that half of the stored energy has been converted to fracture energy.
2. The kinetic region ($\dot{\varepsilon}_0 > 25{,}000\ s^{-1}$). In this region, the fragments are formed from cracks that appear at both defect points and intact points. When the strain rate is increased, the cracks initiated at intact locations overwhelm the cracks initiated at defect points. As a result, fragmentation is mainly a kinetic process and the influence of internal defects is negligible. The $\log(\bar{s})$–$\log(\dot{\varepsilon}_0)$ curve is basically a straight line, which is very close to the line we obtained for the intact bar. The failure strength of the bar is approximately the local strength of the intact points, $\sigma_{\max}$(=300 MPa);
3. The defect-controlled region ($250\ s^{-1} < \dot{\varepsilon}_0 < 25{,}000\ s^{-1}$). In this region the fragments are exclusively formed at the defect points. *All* defect points are fully opened in the final stage. In other words, the internal defect distribution completely controls the fragment size. The failure strength within this region is between $\sigma_{\min}$ and $\sigma_{\max}$, exhibiting a rate-hardening trend. Note that the homogeneous, intact material exhibits no rate-dependency of the failure strength in these simulations. Thus the apparent rate-hardening phenomenon observed in Fig. 10b results from the existence of internal defects within the material. This observation agrees with our previous numerical investigation on SiC–N ceramics (Zhou and Molinari, 2004b) and with the generally accepted explanation for experimental observations on such ceramics, albeit in other stress states (Wang and Ramesh, 2004).

Note that the strain-rate span of the defect-controlled region, namely 250–$25{,}000\ s^{-1}$, is subjected to change as the prescribed defect spacing varies. When the defect spacing decreases, the defect-controlled region as a whole will move rightwards to the higher strain-rate region. When the defect spacing increases, this region moves leftwards to the lower region. If the defect spacing is larger than the quasistatic fragment size estimated in Eq. (11), the defect-controlled region eventually swallows the quasistatic region. In this case, the number of quasistatic fragments is smaller than that estimated by using Eq. (11), due to the lack of fracture seeds.

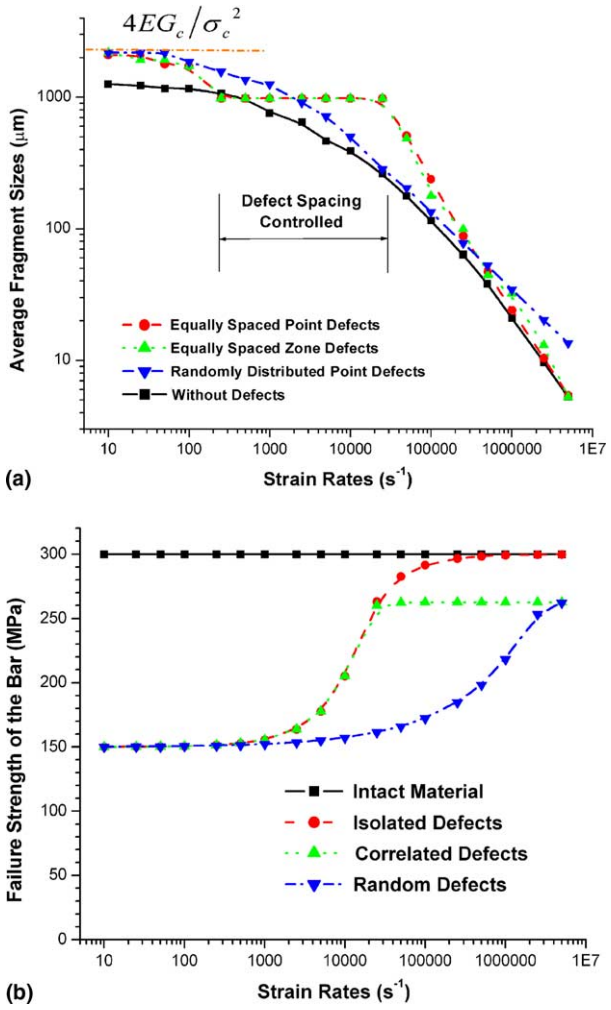

Fig. 10. Average fragment size (a) and macroscopic failure strengths (b) vs. strain rate.

5.1.2. Results for equally-spaced zone defects

We now report the simulation results for the bar with equally-spaced zone defects. The typical history curves of the fragment number N_f and the average stress σ_{ave} are similar to those in the single-point defect case (Fig. 9a–c). The computed $\log(\bar{s})$–$\log(\dot{\varepsilon}_0)$ relationship and the σ_{peak}–$\log(\dot{\varepsilon}_0)$ relationship are plotted as upward triangles in Fig. 10a and b respectively. The dependence of the average fragment size on the strain rate is observed to be essentially identical for the equally-spaced point defects and the equally-spaced zone defects, and there are again three strain-rate regions where the fragmentation process is controlled by a quasistatic mechanism, an internal defect mechanism, and a kinetic mechanism. Fig. 10b shows that the rate-hardening phenomenon is again observed in the defect-distribution controlled strain-rate region, but the failure strength limit (at high rates) for the zone defects is different from that for the point defects. The maximum failure strength for the bar with the zone defects is three quarters between σ_{min} and σ_{max}:

$$\lim_{\dot{\varepsilon}_0 \to \infty} (\sigma_{peak}) = \sigma_{min} + \tfrac{3}{4}(\sigma_{max} - \sigma_{min}). \tag{24}$$

This maximum arises because for the zone defect distribution shown in Fig. 8, the average value of the local material strength is $(\sigma_c)_{ave} = \frac{1}{N+1}\sum_{i=1}^{N+1}\sigma_c(X_i) = \frac{\sigma_{min}+3\sigma_{max}}{4}$. We conclude that as strain rate increases, the failure strength of the bar approaches the average value of the local material strength. This reflects the trend that the bar's failure strength changes from the "*weakest link*" value to the "*average*" value.

5.2. Randomly-distributed point defects

A randomly-distributed point defect model is now considered. In this model, half of the internal nodes (25,000 out of the 50,000) are randomly chosen as internal defects. The local failure strength and the local fracture energy are reduced by a random factor between 50% and 100%, with the strengths and local fracture energies chosen from a uniform strength distribution. Since the failure strength in the uniform (defect-free) bar was 300 MPa, the strengths of the 25,000 "defect" points lie between $\sigma_{min} = 150$ MPa and $\sigma_{max} = 300$ MPa. Note the locations of these defects are now random. The other 25,000 points are intact, with the failure strength $\sigma_{max} = 300$ MPa as before. The calculated $\log(\bar{s})$–$\log(\dot{\varepsilon}_0)$ and σ_{peak}–$\log(\dot{\varepsilon}_0)$ relationships for such a bar with random defects are plotted as the downward triangles in Fig. 10a and b respectively. The $\log(\bar{s}) - \log(\dot{\varepsilon}_0)$ curve of the bar with random defects differs from that of the bar with equal spaced defects in three ways. First, though not shown in Fig. 10a, the average fragment size increases (for the bar with random defects) to up to half of the specimen length if the strain rate is extremely low ($\dot{\varepsilon}_0 < 10^{-3}\ s^{-1}$). In other words, no quasistatic fragment size as expressed by (11) exists. Although there is enough strain energy to form multiple fracture surfaces, the lack of crack seeds prevented nucleation of these cracks in this case. Secondly, the current $\log(\bar{s})$–$\log(\dot{\varepsilon}_0)$ curve for the bar with random defects is a smoothly decreasing curve without the defect-interval controlled strain-rate region observed in the equally-spaced-defects case. This is reasonable, as the randomly-distributed defect model has no intrinsic length scale. Finally, in the high strain-rate region, the *average* fragment size is about twice as large as the value in other cases (either without defects, or with equally-spaced defects). The latter observation is particularly interesting, since it implies that at very high loading rates, a bar with randomly-distributed defects breaks into larger pieces (*on average*) than a bar without any defects. A possible explanation is that for a bar with random defects, the fragment size distribution is narrower than that for a homogeneous bar (see the following results), which may result in turn in larger fragment pieces. However, the reasons for this phenomenon are not yet clear and will be the subject of future investigation.

Examining Fig. 10b, we see that the failure strength of the randomly-distributed-defects bar exhibits a *smoothened* rate-hardening effect. As the strain rate increases, the bar's failure strength increases gradually from the *weakest-link strength* (σ_{min}) to the *average material strength, which is again* $((3\sigma_{min} + \sigma_{max})/4)$. Thus the effect of the defect distribution on the failure strength is similar for the randomly-distributed and equally-spaced cases, once the average material strength is considered. Note, however, that the rate-dependence of the failure strength occurs later for the randomly-distributed case, and builds up over a larger range of strain rates.

The fragment size distributions are now presented for the case of the bar with randomly-distributed defects. The fragment sizes for six strain-rate cases corresponding to $10^2\ s^{-1}$, $5\times10^2\ s^{-1}$, $10^4\ s^{-1}$, $5\times10^4\ s^{-1}$, $10^6\ s^{-1}$, and $5\times10^6\ s^{-1}$ were collected for statistical analysis. The total fragment number from these six numerical tests is 5567. Fig. 11a plots the normalized cumulative fragment number $(\widetilde{\Phi}/N_f)$ against the normalized fragment size $(s/\bar{s})$. These points are best fitted with a curve expressed by Eq. (22), with fitting parameters of $a = 0.18$, $n = 2.65$. Fig. 11b plots the unified probabilistic density function expressed by Eq. (23), in comparison with the numerical test data. A good agreement between the theoretical model and the numerical data is obtained. Several other observations follow:

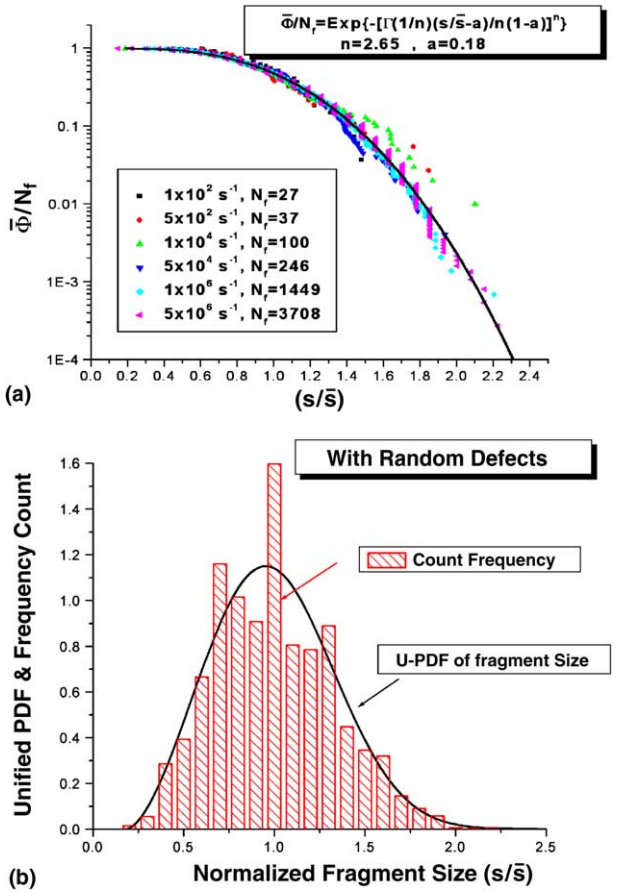

Fig. 11. Statistics of fragment sizes in a bar with random defects: (a) normalized cumulative fragment numbers; (b) normalized fragment size distribution.

1. The span of the normalized fragment size is narrower in a bar with randomly-distributed defects than that in the homogeneous bar. This results in a larger fitting parameter n. The normalized minimum fragment size $a = s_0/\bar{s}$ is smaller than that in the homogenous case.
2. The numerical data points, in all six strain-rate cases, are very close to the fitting curve. This means that the function we proposed for the cumulative fragment size, Eq. (22), describes effectively fragment size characteristics of a bar with random defects. Interestingly, one notes that in many respects, the fit is better when including defects than without doing so.

6. Discussion

The main results of this paper are on the rate-dependencies of both the fragment size and the fragment size distributions. The rate-dependence of fragment size is shown in Fig. 3. Our relationship differs from both the Glenn–Chudnovsky theory and the Grady theory. In the quasistatic region our fragment size is about twice the Glenn–Chudnovsky estimate, because of the stress wave propagation incited by the sudden unloading. In

the very high strain-rate region our fragment size is about one quarter of Grady's estimate. The reasons for this latter difference are still being investigated. We conjecture that during the cohesive fracture process, external work and global kinetic energy are consistently being converted into energy available for failure. The internal impacts between fragments may facilitate this energy conversion process, resulting in the further breakdown of large fragments. The size distributions may also play a role in the fragmentation process.

Our investigations on the sizes of the fragments show that the cumulative fragment numbers under different strain rates can be normalized into a master curve. This means that the fracture points along the bar, though randomly distributed, observe a statistical law. The random fracture point locations along a homogeneous bar come from numerical fluctuations, while those along a randomly-defected bar come from internal defects. Compared to the homogeneous bar, the randomly defected bar exhibits a smoother cumulative fragment number curve and a narrower size distribution. This suggests that the white-noise defect distribution helps smoothen the numerical fluctuations. Note that in this paper only a model ceramic system with idealized defect distributions are studied. However, it is not difficult to adapt the current methodology to study real materials with realistic defect/microstructure properties.

The similarity of the fragment size distribution under different strain rates is of fundamental importance. We can now predict the number of fragments that a brittle bar will break into under a given strain rate. Further, with a unified fragment size distribution function at hand, the sizes of these fragments are readily estimated. Although in practice, loading conditions, internal defects, two-dimensional or three-dimensional fracture, etc. may finally influence the fragmentation process, the above analysis at least provides qualitative predictions of the fragmentation phenomenon.

The bars with initial defect distributions exhibit a rate-hardening property. This suggests that if the other conditions are identical, the failure strength of a heterogeneous material is more strain-rate dependent than the one corresponding to a homogeneous material. One simple way to understand this apparent "rate-hardened strength" is: brittle materials lose some *defect sensitivity* and therefore exhibit increased strength under dynamic loading. The fact that the Weibull parameter influences the apparent rate-dependence of failure strength was first pointed out by Grady and Kipp (1980). Lankford and Blanchard (1991) used this theory to analyze their experimental results. Similar results have been obtained by Denoual and Hild (2000) and Hild et al. (2003) through a probabilistic damage model, and by Zhou and Molinari (2004b) through finite element simulations.

It is informative to compare our analysis with Shenoy and Kim (2003) work. Although both analyses share common points, there exist significant differences between them. The largest difference is that in Shenoy and Kim's approach, the locations of defects are prescribed and are modeled as cohesive node-couples at the very onset of loading, while in our approach the crack points are dynamically nucleated at any possible point. The use in Shenoy and Kim (2003) of an exponential-type cohesive law brings additional flexibility to the system and it was of interest to test the effect of a different, and in some way more robust, cohesive model on fragmentation. It should be added that Shenoy and Kim assumed that during the unloading process, the cohesive opening distance is fixed, so that their partially opened cracks can never close or contact. Our simulations show that the closure, contact, and internal impacts can be important mechanisms in the fragmentation and energy transformation processes. While Shenoy and Kim did not report results at lower strain rates, their "fragment size vs. strain rate" curves in the high strain-rate region are similar to ours. The shape of fragment size distributions is also similar to ours. Shenoy and Kim developed an alternate approach called the dynamic mean field theory (DMFT). However, their fragment size distribution is not directly amenable to comparison. As the DMFT is based on the assumptions that the average (global) stress controls the growth behavior of each individual (local) crack, its fragment size results are somewhat deviated from the exact solution (by a factor 2–1/2). In our research, the solution strategy is straightforward and purely numerical; all unknown quantities are defined at discrete nodes and are solved by a unified algorithm along the time axis. This strategy is highly efficient; therefore there is no need to make further assumptions for approximate averaging analysis.

7. Conclusions

In this paper we have developed a comprehensive methodology to analyze the fragmentation process in a one-dimensional bar. The approach combines the elastic wave interaction process with the cohesive crack opening process. Finite difference schemes along the characteristic lines are employed to obtain the solution. Mechanisms such as local strength distribution, dynamic crack initiation, crack opening/closing/contact behavior, etc., are considered in the analysis.

The methodology has been applied to a model ceramic bar to systematically analyze its fragmentation properties. The deformation of the bar spans a broad strain-rate region, from quasistatic to the very high strain-rate cases. Critical issues such as average fragment size, fragment size distribution, failure strength of the bar, influence of strain rate, influence of internal defect distribution, etc., are addressed. The major conclusions drawn from these analyses are listed as follows:

1. The average fragment size $\bar{s}$ decreases with strain rate $\dot{\varepsilon}_0$. In the very high $\dot{\varepsilon}_0$ region $\bar{s}$ is about 5 times smaller than the Grady's model estimate. In the quasistatic $\dot{\varepsilon}_0$ region $\bar{s}$ is twice larger than the Glenn and Chudnovsky's estimate.
2. The cumulative fragment number function, $\Phi(s)$, changes with $\dot{\varepsilon}_0$. However, when $\bar{s}$ is normalized by the average size $\bar{s}(\dot{\varepsilon}_0)$, and Φ is normalized by $N_f(\dot{\varepsilon}_0) = L/\bar{s}(\dot{\varepsilon}_0)$, the curves collapse onto a master curve. We propose a unified exponential-type cumulative fragment number function (Eq. (21)) that fits numerical data for all strain-rate cases. By differentiation, a unified probabilistic density function (UPDF) of the fragment size (Eq. (23)) is obtained.
3. Internal defect distributions influence significantly the fragmentation process. One direct result of the internal defects is the apparent rate-hardening of the material. As strain rate increases, the failure strength of the bar increases from the weakest-link strength in the quasistatic region to the average material strength in the very high strain-rate region.
4. If the internal defects are equally spaced along the bar, and the defect interval is smaller than the quasistatic fragment size estimated by Eq. (11), then the $\bar{s}$–$\dot{\varepsilon}_0$ relationship can be divided into three parts. In the quasistatic strain-rate region, the average fragment size is approximately the value calculated by Eq. (11). In the intermediate strain-rate region the average fragment size is exactly the interval between fragments. In the very high strain-rate region, the internal defects have little effect on the average fragment size, and the kinetic deformation process controls the fragmentation process.
5. Materials with randomly-distributed defects exhibit smooth, continuous $\bar{s}$–$\dot{\varepsilon}_0$ relationship and a smooth rate-hardening effect. The distributions of the fragment sizes are narrower than the homogeneous materials. The proposed UPDF characterizes the fragment size distribution very well.

This methodology can be conveniently adapted to other physical problems, such as the elastic–plastic fragmentation, materials with realistic microstructures, and stochastic failure phenomena. Research investigating the influence of material parameters and grain-boundaries on the fragmentation process is currently underway.

Acknowledgments

The authors would like to thank Dr. T.W. Wright of the Army Research Laboratory for fruitful discussions. The comments of the anonymous reviewers are also appreciated. This work was performed under the auspices of the Center for Advanced Metallic and Ceramic Systems at Johns Hopkins. The research was sponsored by the Army Research Laboratory (ARMAC-RTP) and was accomplished under the ARMAC-RTP Cooperative Agreement Number DAAD19-01-2-0003. The views and conclusions

contained in this document are those of the authors and should not be interpreted as representing the official policies, either expressed or implied, of the Army Research Laboratory or the US Government. The US Government is authorized to reproduce and distribute reprints for Government purposes not withstanding any copyright notation hereon.

Appendix A. Finite difference scheme along characteristic lines

A.1. Spatial-time discretion

The bar is discretized into $N+1$ nodes spaced by constant interval ΔX ($\Delta X = L/N$). Any unknown variable f (stress, velocity, etc.) is defined at the nodes:

$$f(X_i, t) = f_i(t) \ldots \quad (i = 0, 1, 2, \ldots, N). \tag{A.1}$$

The unknown quantities are calculated by integration from time zero along the time axis. The integration time step is taken as Δt, $\Delta t = \Delta X/c$, where $c = \sqrt{E/\rho}$ is the elastic wave speed, ρ the mass density. In this way the X–t plane is discreted into a rectangular mesh $\Delta X \times \Delta t$. The nodes of the mesh are connected by the characteristic lines observing $\mathrm{d}X/\mathrm{d}t = \pm c$. Having calculated all the variables at the current time step t, the stress and velocity at a node at the next time step $t + \Delta t$ can be solved by using the elastodynamic equations and the cohesive law.

A.2. Solutions of intact nodes

If the internal node i ($0 < i < N$) is not broken, at the next time step:

$$\begin{aligned} \sigma_i(t+\Delta t) &= \frac{\sigma_{i-1}(t) + \sigma_{i+1}(t)}{2} + \frac{\rho c}{2}[v_{i+1}(t) - v_{i-1}(t)] \\ v_i(t+\Delta t) &= \frac{v_{i-1}(t) + v_{i+1}(t)}{2} + \frac{1}{2\rho c}[\sigma_{i+1}(t) - \sigma_{i-1}(t)] \quad (i = 1, 2, \ldots, N-1). \end{aligned} \tag{A.2}$$

The boundary nodes ($i = 0$, or $i = N$) are specifically treated by using the boundary conditions Eq. (2). The stress and velocity at these nodes are

$$\begin{aligned} &\sigma_0(t+\Delta t) = \sigma_1(t) - \rho c[v_{\mathrm{L}} - v_1(t)], \\ &v_0(t+\Delta t) = v_{\mathrm{L}}, \end{aligned} \tag{A.3}$$

$$\begin{aligned} &\sigma_N(t+\Delta t) = \sigma_{N-1}(t) + \rho c[v_{\mathrm{R}} - v_{N-1}(t)], \\ &v_N(t+\Delta t) = v_{\mathrm{R}}. \end{aligned} \tag{A.4}$$

A.3. Solutions of broken nodes

All internal nodes are prone to be broken. When an intact node i nucleates as a crack, it breaks into a pair of points: i^- and i^+. The superscripts "$-$" and "$+$" denote the point to the left and to the right respectively. The two points (i^-, i^+) have identical stress (σ_i), but different velocities (v_{i^-}, v_{i^+}) and spatial locations (x_{i^-}, x_{i^+}). The cohesive opening distance is: $\delta^i_{\mathrm{coh}} = x_{i^+} - x_{i^-}$.

The numerical scheme to solve an internal cracked node is illustrated in Fig. A.1. The two neighboring nodes $i-1$ and $i+1$ may also be cracked nodes. According to the compatibility relationship along the characteristic lines, we have:

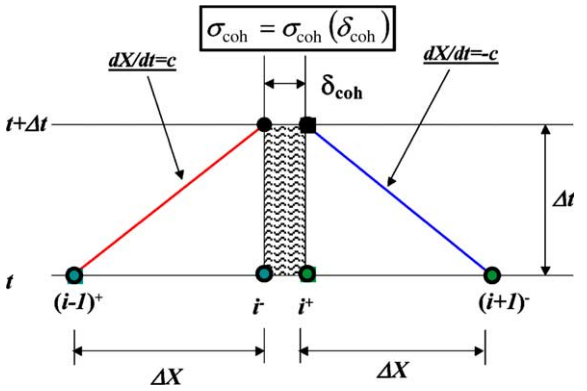

Fig. A.1. Numerical scheme to solve for the state of an internal cracked point.

$$\sigma_i(t+\Delta t) - \sigma_{i-1}(t) = \rho c \lfloor v_{i^-}(t+\Delta t) - v_{(i-1)^+}(t) \rfloor, \tag{A.5}$$

$$\sigma_i(t+\Delta t) - \sigma_{i+1}(t) = -\rho c \lfloor v_{i^+}(t+\Delta t) - v_{(i+1)^-}(t) \rfloor. \tag{A.6}$$

The cohesive law is

$$\sigma_i(t+\Delta t) = \sigma_{coh} \lfloor \delta^i_{coh}(t+\Delta t) \rfloor. \tag{A.7}$$

The cohesive crack opening distance, calculated by the second order difference scheme, is

$$\delta^i_{coh}(t+\Delta t) = \delta^i_{coh}(t) + \frac{\Delta t}{2}\{[v_{i^+}(t+\Delta t) + v_{i^+}(t)] - [v_{i^-}(t+\Delta t) + v_{i^-}(t)]\}. \tag{A.8}$$

From the above four algebraic equations (A.5)–(A.8), the four unknown quantities at time $t+\Delta t$: $\sigma_i(t+\Delta t)$, $v_{i^-}(t+\Delta t)$, $v_{i^+}(t+\Delta t)$, and $\delta^i_{coh}(t+\Delta t)$, can be solved.

A.4. Fully broken nodes and closed nodes

If a cracked node completely fails, it can no longer sustain any tensile stress. In this case the point is treated as a free interface as long as it has positive crack opening displacement ($\delta_{coh} > 0$). On the other hand, if a partially or fully opened crack closes up completely, the two points that were separated are brought into contact again ($\delta_{coh} = 0$). In this situation, internal impact occurs, resulting in compressive stress. In this case we tie up the two points of the cohesive crack, and use the velocity continuity relationship, $v_{i^-}(t+\Delta t) = v_{i^+}(t+\Delta t)$ to solve for the stress and velocity of the closed crack point. Physically, the contacted crack point is equivalent to an intact point that allows a compressive wave to pass through, so that Eq. (A.2) is again applied to compute its stress and velocity.

Appendix B. Calibrations of simulation

B.1. Effect of mesh density

Test calculations were conducted to study the effect of mesh density. We consider a bar of length $L = 50$ mm under $\dot{\varepsilon}_0 = 10^5\ s^{-1}$ (the high strain rates are the most critical as the cohesive fracture process is very short, and so the time-step must be small enough to resolve this almost instantaneous process).

The material parameters are the same as listed in Section 3. The total number of discrete points is 2501, 5001, 10,001, 25,001, 50,001, and 100,001. The mesh densities are 50 mm^{-1}, 100 mm^{-1}, 200 mm^{-1}, 500 mm^{-1}, 1000 mm^{-1}, and 2000 mm^{-1}, respectively. We plot the number of the fragments as functions of time in Fig. B.1(a). This number starts from 1, increases rapidly after the bar fractures, and saturates at the final fragment number N_f. Fig. B.1(b) shows N_f and the average fragment size s_f ($s_f = L/N_f$) as functions of the mesh density. A trend that N_f decreases with the increase of the segment (mesh) density is observed, but when the segment density is larger than 1000 mm^{-1} ($\Delta X = 1$ μm), the calculation results are convergent. It seems that the observed "mesh-dependence" comes from numerical errors, where a small segment density represents coarse mesh and large time step. In our investigation, we chose the fixed discretization of $\Delta X = 1$ μm with $\Delta t = 0.1$ ns for the numerical calculations.

B.2. Effect of sample length

The length of the bar L should be large enough so that many fragments are formed, so that the number of fragment samples can demonstrate a meaningful statistical property. To determine the adequate sample

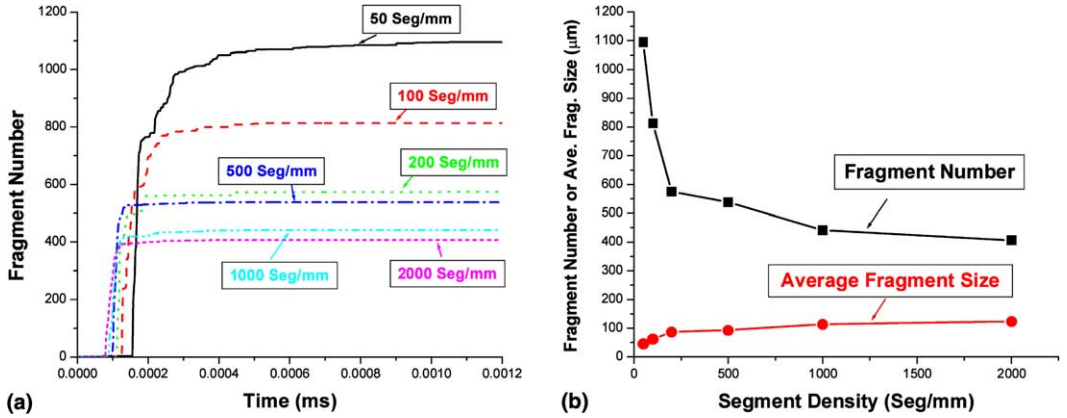

Fig. B.1. Effects of mesh density on fragmentation, and consequent definition of sufficient mesh density: (a) fragment number vs. time for various mesh densities; (b) dependences of N_f and s_f on mesh density.

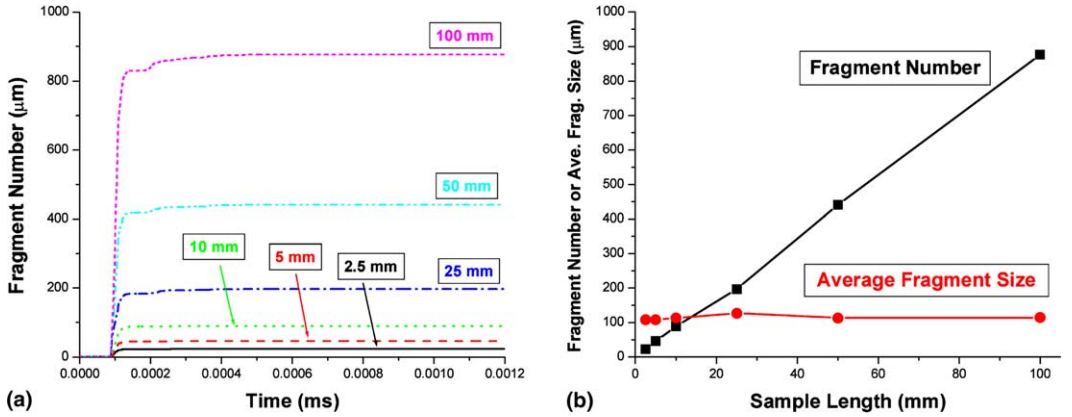

Fig. B.2. Effects of sample length on fragment size and fragment number: (a) fragment number vs. time for different sample lengths; (b) dependence of N_f and s_f on sample length.

length, we computed for bars with different lengths: $L = 2.5$ mm, 5 mm, 10 mm, 25 mm, 50 mm, and 100 mm. All the bars are discretized with a mesh size $\Delta X = 1$ μm and are under $\dot{\varepsilon}_0 = 10^5\ \mathrm{s}^{-1}$. Fig. B.2(a) plots the time histories of the total fragment number for the different bar lengths. The saturated fragment number N_f and the average fragment size $\bar{s}$ are plotted against sample length in Fig. B.2(b). The average fragment sizes are approximately the same for all bars. This means that the length of the bar, when above 2.5 mm, has little effect on the average fragment length. However, as we estimate fewer fragments when the strain rate decreases to the quasistatic region, we chose the 50 mm bar as the standard sample.

Appendix C. Energy models of fragmentations in 1D, 2D, and 3D cases

Here we neglect the strain energy effect. Fig. C.1 shows three fragments in different dimensions: a 1D bar of unit cross-section area, a 2D cylinder of unit length, and a 3D sphere. The dimension of each fragment (the length for the bar, or the diameters for the cylinder and the sphere) is d. The volumes and the surfaces of these fragments are

$$V = \begin{cases} d & (1\mathrm{D}), \\ \pi d^2/4 & (2\mathrm{D}), \\ \pi d^3/6 & (3\mathrm{D}), \end{cases} \tag{C.1.1}$$

$$S = \begin{cases} 2 & (1\mathrm{D}), \\ \pi d & (2\mathrm{D}), \\ \pi d^2 & (3\mathrm{D}). \end{cases} \tag{C.1.2}$$

Each fragment expands at a uniform linear strain rate $\dot{\varepsilon} = \dot{d}/d$. The volume strain rate $\dot{V}/V$ and the relative density rate $\dot{\rho}/\rho$ are expressed as

$$\frac{\dot{V}}{V} = \left(-\frac{\dot{\rho}}{\rho}\right) = \begin{cases} \dot{\varepsilon} & (1\mathrm{D}), \\ 2\dot{\varepsilon} & (2\mathrm{D}), \\ 3\dot{\varepsilon} & (3\mathrm{D}). \end{cases} \tag{C.2}$$

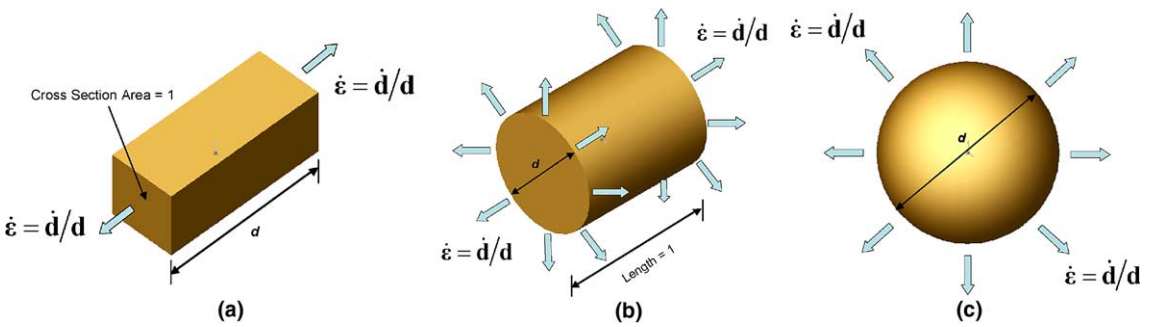

Fig. C.1. Expansions of (a) a 1D bar; (b) a 2D cylinder; (c) a 3D sphere.

As the fragments are expanding outward uniformly, the material velocity relative to the center of each fragment is linearly distributed, as

$$v(x) = r\dot{\varepsilon}, \quad \begin{array}{l} r \in [-d/2, d/2] \text{ (1D)}, \\ r \in [0, d/2] \text{ (2D or 3D)}, \end{array} \tag{C.3}$$

and the *local* kinetical energy relative to the mass center can be evaluated as

$$T' = \begin{cases} \int_{-d/2}^{d/2} \frac{1}{2}(r\dot{\varepsilon})^2 \rho \, \mathrm{d}r = \frac{1}{24}\rho\dot{\varepsilon}^2 d^3 & \text{(1D)}, \\ \int_{0}^{d/2} \frac{1}{2}(r\dot{\varepsilon})^2 \rho (2\pi r) \, \mathrm{d}r = \frac{1}{64}\rho\dot{\varepsilon}^2 \pi d^4 & \text{(2D)}, \\ \int_{0}^{d/2} \frac{1}{2}(r\dot{\varepsilon})^2 \rho (4\pi r^2) \, \mathrm{d}r = \frac{1}{80}\rho\dot{\varepsilon}^2 \pi d^5 & \text{(3D)}. \end{cases} \tag{C.4}$$

On the other side, the surface energy of the fragments are calculated using (C.1.2):

$$\Gamma = S\gamma_c = \begin{cases} 2\gamma_c = G_c & \text{(1D)}, \\ \pi \mathrm{d}\gamma_c = \frac{\pi \mathrm{d} G_c}{2} & \text{(2D)}, \\ \pi \mathrm{d}^2 \gamma_c = \frac{\pi \mathrm{d}^2 G_c}{2} & \text{(3D)}, \end{cases} \tag{C.5}$$

where γ_c is the surface energy that is half of the fracture energy G_c: $\gamma_c = G_c/2$.

C.1. The minimum total energy density theory

There exist two energy theories to estimate the fragment size. In the first theory, it is assumed that when a fragment is created, its total energy density, namely $(T' + \Gamma)/V$ takes the minimum (Grady, 1982). By substituting (C.4), (C.5) and (C.1.1) into the stationary condition: $\frac{\partial[(T'+\Gamma)/V]}{\partial d} = 0$, and with some mathematical manipulations, we obtain:

$$d = \begin{cases} \left(\frac{12G_c}{\rho\dot{\varepsilon}^2}\right)^{1/3} & \text{(1D)}, \\ \left(\frac{16G_c}{\rho\dot{\varepsilon}^2}\right)^{1/3} & \text{(2D)}, \\ \left(\frac{20G_c}{\rho\dot{\varepsilon}^2}\right)^{1/3} & \text{(3D)}. \end{cases} \tag{C.6}$$

C.2. The energy balance theory

According to this theory, when fragmentation happens, the local kinetical energy is converted into the surface energy. By substituting (C.4) and (C.5) into the energy balance condition: $T' = \Gamma$, we can obtain:

$$d = \begin{cases} \left(\frac{24G_c}{\rho\dot{\varepsilon}^2}\right)^{1/3} & \text{(1D)}, \\ \left(\frac{32G_c}{\rho\dot{\varepsilon}^2}\right)^{1/3} & \text{(2D)}, \\ \left(\frac{40G_c}{\rho\dot{\varepsilon}^2}\right)^{1/3} & \text{(3D)}. \end{cases} \tag{C.7}$$

Note that the fragment sizes estimated by the energy balance theory are $\sqrt[3]{2} \approx 1.26$ times the minimum energy density estimates. In either problem the fragment size scales with strain rate by the $(-2/3)$ power. The 1D case of the energy balance theory, i.e. the first equation in (C.7) is what we write as Eq. (7) in the paper. Eqs. (8) and (9) can be deduced similarly with the consideration of the strain energy term (Miller et al., 1999).

References

Camacho, G.T., Ortiz, M., 1996. Computational modelling of impact damage in brittle materials. Int. J. Solids Struct. 33, 2899–2938.
Denoual, C., Hild, F., 2000. A damage model for the dynamic fragmentation of brittle solids. Comput. Methods Appl. Mech. Eng. 183, 247–258.
Drugan, W.J., 2001. Dynamic fragmentation of brittle materials: analytical mechanics-based models. J. Mech. Phys. Solids 49, 1181–1208.
Espinosa, H.D., Zavattieri, P.D., Dwivedi, S.K., 1998. A finite deformation continuum/discrete model for the description of fragmentation and damage brittle materials. J. Mech. Phys. Solids 46, 1909–1942.
Glenn, L.A., Chudnovsky, A., 1986. Strain-energy effects on dynamic fragmentation. J. Appl. Phys. 59, 1379–1380.
Grady, D.E., 1982. Local inertial effects in dynamic fragmentation. J. Appl. Phys. 53, 322–325.
Grady, D.E., 1990. Particle size statistics in dynamic fragmentation. J. Appl. Phys. 68, 6099–6105.
Grady, D.E., Kipp, M.E., 1980. Continuum modelling of explosive fracture in oil shale. Int. J. Rock Mech. Mining Sci. Geomech. Abstract 17, 147–157.
Grady, D.E., Kipp, M.E., 1985. Geometric statistics and dynamic fragmentation. J. Appl. Phys. 58, 1210–1222.
Hild, F., Denoual, C., Forquin, P., Brajer, X., 2003. On the probabilistic–deterministic transition involved in a fragmentation process of brittle materials. Comput. Struct. 81, 1241–1253.
Lankford, J., Blanchard, C.R., 1991. Fragmentation of brittle materials at high rates of loading. J. Mater. Sci. 26, 3067–3072.
Miller, O., Freund, L.B., Needleman, A., 1999. Modeling and simulation of dynamic fragmentation in brittle materials. Int. J. Fract. 96, 101–125.
Pandolfi, A., Krysl, P., Ortiz, M., 1999. Finite element simulation of ring expansion and fragmentation: the capturing of length and time scales through cohesive models of fracture. Int. J. Fract. 95, 279–297.
Shenoy, V.B., Kim, K.-S., 2003. Disorder effects in dynamic fragmentation of brittle materials. J. Mech. Phys. Solids 51, 2023–2035.
Wang, H., Ramesh, K.T., 2004. Dynamic strength and fragmentation of hot-pressed silicon carbide under uniaxial compression. Acta Mater. 52, 355–367.
Weibull, W., 1939a. The phenomenon of rupture in solids. In: Proceedings of the Royal Swedish Institute for Engineering Research, p. 153.
Weibull, W., 1939b. A statistical theory of the strength of materials. In: Proceedings of the Royal Swedish Institute for Engineering Research, p. 151.
Weibull, W., 1951. A statistical distribution function of wide applicability. J. Appl. Mech. 18, 293–297.
Xu, X.-P., Needleman, A., 1994. Numerical simulations of fast crack growth in brittle solids. J. Mech. Phys. Solids 42, 1397–1434.
Xu, X.-P., Needleman, A., 1996. Numerical simulations of dynamic crack growth along an interface. Int. J. Fract. 74, 289–324.
Zhou, F., Molinari, J.-F., 2004a. Dynamic crack propagation with cohesive elements: a methodology to address mesh dependency. Int. J. Numer. Methods Eng. 59, 1–24.
Zhou, F., Molinari, J.-F., 2004b. Stochastic fracture of ceramics under dynamic tensile loading. Int. J. Solids Struct. 41, 6573–6596.